



## Updated Search for the Standard-Model Higgs Boson in the $ZH \rightarrow \nu\bar{\nu}b\bar{b}$ Channel in $9.5 \text{ fb}^{-1}$ of $p\bar{p}$ Collisions at $\sqrt{s} = 1.96 \text{ TeV}$

The DØ Collaboration  
URL: <http://www-d0.fnal.gov>

(Dated: July 2, 2012)

A search is performed for the standard-model Higgs boson in  $9.5 \text{ fb}^{-1}$  of  $p\bar{p}$  collisions at  $\sqrt{s} = 1.96 \text{ TeV}$ , collected with the DØ detector at the Fermilab Tevatron Collider. The final state considered contains a pair of  $b$  jets and is characterized by an imbalance in transverse energy, as expected from  $p\bar{p} \rightarrow ZH \rightarrow \nu\bar{\nu}b\bar{b}$  production. The search is also sensitive to the  $WH \rightarrow \ell\nu b\bar{b}$  channel when the charged lepton is not identified. For a Higgs-boson mass of 115 GeV (125 GeV), a limit is set at the 95% C.L. on the cross section  $\sigma(p\bar{p} \rightarrow [Z/W]H)$ , assuming standard-model branching fractions, that is a factor of 3.0 (4.3) larger than the theoretical standard-model value, for an expected factor of 2.7 (3.9). The search is also reinterpreted as a search for  $WZ$  and  $ZZ$  production, resulting in a measurement of the combined cross section that is a factor of  $0.94 \pm 0.31(\text{stat}) \pm 0.34(\text{syst})$  relative to the standard-model prediction, and with an observed significance of  $2.0 \sigma$ , consistent with the expected significance of  $2.1 \sigma$ .

*Preliminary Results for 2012 Summer Conferences*

## I. INTRODUCTION

The existence of the Higgs boson is the only fundamental element of the standard model (SM) that has yet to be confirmed. Its observation would be a key step in establishing the mechanism of electroweak symmetry breaking and mass generation. Associated  $ZH$  production in  $p\bar{p}$  collisions, with  $Z \rightarrow \nu\bar{\nu}$  and  $H \rightarrow b\bar{b}$ , is among the most sensitive processes for seeking a Higgs boson with a mass  $m_H \lesssim 135$  GeV at the Fermilab Tevatron Collider [1]. The D0 Collaboration published a search for this process based on  $5.2 \text{ fb}^{-1}$  of integrated luminosity [2]. A lower limit of 114.4 GeV was set by the LEP experiments on the mass of the Higgs boson from searches for the reaction  $e^+e^- \rightarrow ZH$  [3], while an upper limit at 127 GeV has been recently established by the LHC experiments [4, 5]. These limits and those given below are all defined at the 95% confidence level (C.L.).

The final-state topology considered in this search consists of a pair of  $b$  jets from  $H \rightarrow b\bar{b}$  decay and missing transverse energy ( $\cancel{E}_T$ ) from  $Z \rightarrow \nu\bar{\nu}$ . The search is also sensitive to the  $WH$  process when the charged lepton from  $W \rightarrow \ell\nu$  decay is not identified. The main backgrounds arise from  $(W/Z)$ +heavy-flavor jets (jets initiated by  $b$  or  $c$  quarks), top-quark production, and multijet (MJ) events with  $\cancel{E}_T$  arising from mismeasurement of jet energies.

To validate the techniques used in the search for the Higgs boson, the analysis is reinterpreted as a measurement of  $WZ$  and  $ZZ$  diboson production. The only modification is in the training of the final multivariate discriminant, for which a diboson signal is used instead of a Higgs signal.

Compared to the previous results obtained with the same amount of data [6], the sensitivity of the search for the Higgs boson has improved by  $\sim 10\%$ . This is essentially due to the increased Monte Carlo statistics used in the training of the final discriminants.

## II. DATA AND SIMULATED SAMPLES

The D0 detector is described in Ref. [7]. The data used in this analysis were recorded using triggers designed to select events with jets and  $\cancel{E}_T$  [8]. After imposing data quality requirements, the total integrated luminosity recorded with those triggers is  $9.5 \text{ fb}^{-1}$ , which corresponds to the full Run II dataset.

The Tevatron Run II data taking is split into two periods, one prior to March 2006 which is referred to as Run IIa, while the period after is referred to as Run IIb. This division corresponds to the installation of an additional layer of silicon vertex detector, trigger upgrades, and a significant increase in the rate of delivered luminosity. The Run IIb period is further divided into three to reflect increases in the rate of delivered luminosity or changes in the detector performance. The data are modeled in each of these periods using dedicated Monte Carlo (MC) samples.

The analysis relies on (i) charged particle tracks, (ii) calorimeter jets reconstructed in a cone of radius 0.5 using the iterative midpoint cone algorithm [9], and (iii) electrons or muons identified through the association of tracks with electromagnetic calorimeter clusters or with hits in the muon detector, respectively. The  $\cancel{E}_T$  is reconstructed as the opposite of the vectorial sum of transverse components of energy deposits in the calorimeter and is corrected for identified muons. Jet energies are calibrated using transverse energy balance in photon+jet and  $Z$ +jet events [10], and these corrections are propagated to the  $\cancel{E}_T$ .

Those backgrounds arising from MJ processes with instrumental effects giving rise to missing transverse energy are estimated from data. The remainder of the SM backgrounds and the signal processes are simulated by MC. Events from  $(W/Z)$ +jets processes are generated with ALPGEN [11], interfaced with PYTHIA [12] for initial and final-state radiation and for hadronization. The  $p_T$  spectrum of the  $Z$  boson is reweighted to match the D0 measurement [13]. The  $p_T$  spectrum of the  $W$  boson is reweighted using the same experimental input, corrected for the differences between the  $Z$  and  $W$   $p_T$  spectra predicted in next-to-next-to-leading order (NNLO) QCD [14]. For  $t\bar{t}$  and electroweak single top quark production, the ALPGEN and SINGLETOP [15] generators, respectively, are interfaced with PYTHIA, while vector boson pair production is generated with PYTHIA. The  $ZH$  and  $WH$  signal processes are generated with PYTHIA for Higgs-boson masses ( $m_H$ ) from 100 to 150 GeV in 5 GeV steps. All these simulations use CTEQ6L1 parton distribution functions (PDFs) [16].

The absolute normalizations for  $(W/Z)$  inclusive production are obtained from NNLO calculations of total cross sections based on Ref. [17], using the MRST2004 NNLO PDFs [18]. The heavy-flavor fractions in  $(W/Z)$ +jets are obtained using MCFM [19] at next-to-leading order (NLO). The diboson cross sections are also calculated with MCFM. Cross sections for pair and single top quark production are taken from Ref. [20]. For signal processes, cross sections are taken from Ref. [21].

Signal and background samples are passed through a full GEANT3-based simulation [22] of the detector response and processed with the same reconstruction program as used for data. Events from randomly selected beam crossings are overlaid on simulated events to account for detector noise and contributions from additional  $p\bar{p}$  interactions. Parameterizations of the trigger efficiencies are determined using events collected with independent triggers based on information from the muon detectors. Corrections for residual differences between data and simulation are applied

for electron, muon and jet identification. Jet energy calibration and resolution are adjusted in simulated events to match those measured in data.

### III. EVENT SELECTION

A preselection that greatly reduces the overwhelming background from multijet events is performed as follows. The interaction vertex must be reconstructed within the acceptance of the silicon vertex detector and at least three tracks must originate from that vertex. Jets with associated tracks which meet minimal quality criteria to ensure that the  $b$ -tagging algorithm operates efficiently are denoted as “taggable” jets. Exactly two taggable jets are required of which one must be the leading (highest  $p_T$ ) jet in the event; the Higgs candidate is formed from these two jets, denoted  $\text{jet}_1$  and  $\text{jet}_2$  (ordered in decreasing  $p_T$ ). These jets must have transverse momentum  $p_T > 20$  GeV and pseudorapidity  $|\eta| < 2.5$  ( $\eta = -\ln[\tan(\theta/2)]$ , where  $\theta$  is the polar angle with respect to the proton beam direction). The two taggable jets must not be back-to-back in the plane transverse to the beam direction:  $\Delta\phi(\text{jet}_1, \text{jet}_2) < 165^\circ$ . Finally,  $\cancel{E}_T > 30$  GeV is required.

The Run IIa data taking period had looser triggers which resulted in a larger multijet background component in the analysis. To reduce the multijet background in the Run IIa component of the analysis, two additional requirements are introduced, replicating the additional trigger conditions introduced in Run IIb. These are a requirement on the azimuthal angle between the direction of any jet and the  $\cancel{E}_T$  direction,  $\Delta\phi(\text{any jet}, \cancel{E}_T) > 23^\circ$ , and the requirement  $\cancel{E}_T^{\text{Trig}} > 30$  GeV, where  $\cancel{E}_T^{\text{Trig}}$  is the  $\cancel{E}_T$  as calculated in the trigger without the energy in the outermost hadronic calorimeter taken into account.

Additional selection criteria define four distinct samples: (i) an “analysis” sample used to search for a Higgs-boson signal, (ii) an “electroweak (EW) control” sample, enriched in  $W(\rightarrow \mu\nu)$ +jets events where the jet system has a topology similar to that of the analysis sample, which is used to validate the background MC simulation, (iii) a “MJ-model” sample, dominated by multijet events, used to model the MJ background in the analysis sample, and (iv) a large “MJ-enriched” sample, used to validate this modeling procedure.

The analysis sample is selected by requiring the scalar sum of the transverse momenta of the two leading taggable jets to be greater than 80 GeV,  $\cancel{E}_T > 40$  GeV and a measure of the  $\cancel{E}_T$  significance  $\mathcal{S} > 5$  [23]. Larger values of  $\mathcal{S}$  correspond to  $\cancel{E}_T$  values that are less likely to be caused by fluctuations in jet energies. The  $\mathcal{S}$  distribution is shown for the analysis and EW-control samples in Fig. 1.

The dominant signal topology is a pair of  $b$  jets recoiling against the  $\cancel{E}_T$  due to the neutrinos from  $Z \rightarrow \nu\bar{\nu}$ , therefore with the direction of the  $\cancel{E}_T$  at large angle with respect to the direction of each jet. In contrast, in events from MJ background with fluctuations in jet energy measurement, the  $\cancel{E}_T$  tends to be aligned with a mismeasured jet. An alternate estimate of the missing transverse energy can be obtained from  $\cancel{p}_T$ , the missing  $p_T$  calculated from the reconstructed charged particle tracks. This variable is less sensitive to jet energy measurement fluctuations. In signal events,  $\cancel{p}_T$  is also expected to point away from both jets, while in MJ background its angular distribution is expected to be more isotropic. Advantage is taken from these features through the variable  $\mathcal{D} = (\Delta\phi(\cancel{p}_T, \text{jet}_1) + \Delta\phi(\cancel{p}_T, \text{jet}_2))/2$ . For signal events, as well as for the non-MJ backgrounds, it is expected that  $\mathcal{D} > \pi/2$  in the vast majority of events, whereas the MJ background events tend to be symmetrically distributed around  $\pi/2$ . In the analysis sample,  $\mathcal{D} > \pi/2$  is therefore required. The effectiveness of this criterion can be seen in Fig. 2, where the distribution of  $\mathcal{D}$  is shown for the EW control sample, dominated by events with real  $\cancel{E}_T$ , and for the MJ-enriched sample, dominated by events with  $\cancel{E}_T$  arising from instrumental effects. Details on the selection of these control samples are given below. To improve the efficiency of this criterion for the  $(W \rightarrow \mu\nu)H$  signal with non-identified muons, tracks satisfying tight isolation criteria are removed from the  $\cancel{p}_T$  computation. The reverse of the  $\mathcal{D}$  requirement is also used to define the MJ-model sample, as explained below.

Events containing an isolated electron or muon with  $p_T > 15$  GeV are rejected to ensure orthogonality with the D0  $WH$  search in the lepton+ $\cancel{E}_T$  topology [24].

The EW-control sample is selected in a similar manner to the analysis sample, except that an isolated muon with  $p_T > 15$  GeV is required. The multijet content of this sample is rendered negligible by requiring that the transverse mass of the muon and  $\cancel{E}_T$  system is larger than 30 GeV, and that the  $\cancel{E}_T$ , calculated taking account of the  $\mu$  from the  $W$  decay, is greater than 20 GeV. To ensure similar jet topologies for the analysis and EW-control samples, the  $\cancel{E}_T$ , not corrected for the selected muon, is required to exceed 40 GeV. The number of selected events is in good agreement with the SM expectation. All the kinematic distributions are also well described once reweightings of the distributions of  $\Delta\eta$  between the two taggable jets and of the pseudorapidity of the next-to-leading taggable jet are performed, as suggested by a simulation of  $(W/Z)$ +jets using the SHERPA generator [25]. Four representative distributions in the EW-control sample are shown in Fig. 3.

The MJ-model sample, used to determine the MJ background, is selected in the same manner as the analysis sample, except that the requirement  $\mathcal{D} > \pi/2$  is inverted. The small remaining contributions from non-MJ SM processes in

the  $\mathcal{D} < \pi/2$  region are subtracted, and the resulting sample is used to model the MJ background in the analysis sample. The MJ background in the region  $\mathcal{D} > \pi/2$  is normalized by performing a fit of the sum of the MJ and SM backgrounds to the  $\cancel{E}_T$  distribution of the data in the analysis sample.

The MJ-enriched sample is used to test the validity of this approach and is defined in the same manner as the analysis sample, except that the requirement on  $\mathcal{S}$  is inverted. As a result, the MJ background dominates the entire range of  $\mathcal{D}$  values, and this sample is used to verify that the events with  $\mathcal{D} < \pi/2$  correctly model those with  $\mathcal{D} > \pi/2$ . Representative distributions in the MJ-enriched sample are shown in Fig. 4.

A multivariate  $b$ -tagging discriminant, using several boosted decision trees as inputs, is used to select events with one or more  $b$  quark candidates. This algorithm is an upgraded version of the neural network  $b$ -tagging algorithm described in Ref. [26]. The new algorithm includes more information related to the lifetime of the jet and results in a better discrimination between  $b$  and light ( $u, d, s, g$ ) jets. It provides an output between 0 and 1 for each jet, with a value closer to one indicating a higher probability that the jet originated from a  $b$  quark. The output from the algorithm measured on simulated events is adjusted to match the output measured on dedicated data samples as described in more detail in Ref. [26]. From this continuous output, thirteen operating points ( $L_b$ ) are defined, with untagged jets having  $L_b = 0$  and  $b$  purity increasing with  $L_b$  from 0 to 12. The typical per-jet efficiency and fake rate for the loosest non-zero (tightest)  $b$ -tag operating point are about 80% (50%) and 10% (1%), respectively.

To improve the sensitivity of the analysis, two high signal purity samples are defined from the analysis sample using the variable  $L_{bb} = L_b(\text{jet}_1) + L_b(\text{jet}_2)$ . The two samples are defined as follows:

- a tight  $b$ -tag sample:  $L_{bb} \geq 18$
- a medium  $b$ -tag sample:  $17 \geq L_{bb} \geq 11$

The medium  $b$ -tag sample contains events with two loosely  $b$ -tagged jets, as well as events with one tightly  $b$ -tagged jet and one untagged jet. The signal-to-background ratios for a Higgs-boson mass of 115 GeV in the pre, medium and tight  $b$ -tag samples, after applying a multijet veto (defined in the next section), are respectively 0.05%, 0.4% and 1.5%.

#### IV. ANALYSIS USING DECISION TREES

A stochastic gradient boosted decision tree (DT) technique is employed, as implemented in the TMVA package [27], to take advantage of differences in signal and background processes to improve their separation. First, a “MJ DT” (multijet-rejection DT) is trained to discriminate between signal and MJ-model events before any  $b$  tagging is applied. To avoid any possible Higgs-mass dependence at this stage of the analysis, signal events are not used and the MJ DT is trained on a sample of  $(W/Z) + \text{heavy-flavor jets}$  events instead. Variables that provide some discrimination have been chosen for the MJ DT, excluding those strongly correlated to the Higgs mass (such as the dijet mass itself or the  $\Delta R = \sqrt{\Delta\eta^2 + \Delta\phi^2}$  between  $\text{jet}_1$  and  $\text{jet}_2$ ). The full list of the seventeen input variables to the MJ DT is given in Table I.

The MJ DT output, which ranges between  $-1$  and  $+1$ , is shown for the analysis and EW control samples after the medium  $b$  tagging requirement in Fig. 5. Good agreement is found between data and the predicted background. A value of the multijet discriminant in excess of  $-0.3$  is required (multijet veto), which removes 93% of the multijet background, while retaining 85% of the non-MJ SM backgrounds and 90% of the signal for  $m_H = 115$  GeV. The number of expected signal and background events, as well as the number of observed events, are given in Table II, after imposing the multijet veto. Distributions in the analysis sample after the multijet veto are shown in Fig. 6 before any  $b$ -tagging requirement and in Fig. 7 for  $b$ -tagged events.

Next, to discriminate signal from the other SM backgrounds, two “SM DTs” (SM-background-rejection DTs) are trained for each  $m_H$ , one in the medium  $b$ -tag channel and one in the tight  $b$ -tag channel. Some of the MJ DT input variables are used again, but most of the discrimination comes from additional kinematic variables correlated to the Higgs mass, of which, as expected, the dijet mass has the strongest discriminating power. The full list of variables is shown in Table I. The SM DT outputs, which range between  $-1$  and  $+1$ , are used as final discriminants. Their distributions are shown in Fig. 8 for  $m_H = 115$  GeV.

#### V. SYSTEMATIC UNCERTAINTIES

Experimental uncertainties arise from the integrated luminosity (6.1%) [28], the trigger simulation (2%), the jet energy calibration and resolution (1-2%), jet reconstruction and taggability (3%), the lepton identification (1%), the modeling of the MJ background (25%, which translates into a 1% uncertainty on the total background) and the

$b$ -tagging (from 3.7% for background in the medium  $b$ -tag sample to 7.8% for signal in the tight  $b$ -tag sample). Their impact is assessed on overall normalizations, as shown in Table III, and on the shapes of distributions in the final discriminants. The impact of the uncertainties associated with the corections to the jet angular distributions of the  $(W/Z)$ +jets background is negligible. Correlations among systematic uncertainties in signal and background are taken into account when extracting the final results.

Theoretical uncertainties on cross sections for SM processes are estimated as follows. For  $(W/Z)$ +jets production, an uncertainty of 10% is assigned to the total cross sections and an uncertainty of 20% to the heavy-flavor fractions (estimated from MCFM at NLO [19]). For other SM backgrounds, uncertainties are taken from Ref. [20] or from MCFM, and range from 6% to 10%. The uncertainties on cross sections for signal (7% for  $m_H = 115$  GeV) are taken from Ref. [21]. Uncertainties on the shapes of the final discriminants arise from (i) the modeling of  $(W/Z)$ +jets, assessed by varying the renormalization-and-factorization scale and by comparing results from ALPGEN interfaced with HERWIG [29] to ALPGEN interfaced with PYTHIA, and (ii) the choice of PDFs, estimated using the prescription of Ref. [16].

## VI. LIMIT SETTING PROCEDURE

Agreement is found between data and the predicted background, both in the number of selected events (Table II) and in the distribution of final discriminants (Fig. 8), once systematic uncertainties are taken into account (Table III). A modified frequentist approach [30] is used to set limits on the cross section for SM Higgs-boson production, where the test statistic is a log-likelihood ratio (LLR) for the background-only and signal+background hypotheses. The result is obtained by summing LLR values over the bins in the final discriminants shown in Fig. 8. The impact of systematic uncertainties on the sensitivity of the analysis is reduced by maximizing a “profile” likelihood function [31] in which these uncertainties are given Gaussian constraints associated with their priors. Figure 9 shows a comparison of the SM DT distributions after profiling along with the background-subtracted data and expected signal for the  $m_H = 115$  GeV hypothesis. In this case, the background prediction and its uncertainties have been determined from the fit to data under the background-only hypothesis.

## VII. HIGGS SEARCH RESULTS

The results are given in terms of LLR values in Fig. 10(a) and as limits in Table IV and Fig. 10(b). For  $m_H = 115$  GeV (125 GeV), the observed and expected limits on the combined cross section of  $ZH$  and  $WH$  production are factors of 3.0 (4.3) and 2.7 (3.9) larger than the SM value, respectively.

## VIII. DIBOSON SEARCH RESULTS

The final states arising from  $(Z \rightarrow \nu\bar{\nu})Z$  and  $(W \rightarrow \ell\nu)Z$  production with  $Z \rightarrow b\bar{b}$  are similar to those used for the Higgs-boson search reported above. Evidence for  $ZZ$  and  $WZ$  production can therefore be used to validate the techniques employed in the Higgs-boson search. The only modification to the analysis is in the training of the final discriminants, where  $ZZ$  and  $WZ$  are now treated as signal with the remaining diboson process,  $WW$ , kept as background. The medium and tight  $b$ -tag SM DTs are shown in Fig. 11.

A cross-section scale factor of  $0.94 \pm 0.31(stat) \pm 0.34(syst)$  is measured with respect to the predicted standard-model value of 4.95 pb, with an observed significance of  $2.0\sigma$  ( $2.1\sigma$  expected). Figure 12 shows a comparison of the SM DT distributions, along with the background-subtracted data, after the background prediction and its uncertainties have been determined from a fit to the data under the signal+background hypothesis.

The measurement of the diboson cross section has also been carried out using the dijet invariant mass as final discriminant (as opposed to the SM DT). A cross-section scale factor of  $1.08 \pm 0.35(stat) \pm 0.39(syst)$  is measured with respect to the predicted standard-model value, with an observed significance of  $2.0\sigma$  ( $1.9\sigma$  expected). Figure 13 shows a comparison of the dijet invariant mass distributions, along with the background-subtracted data, after the background prediction and its uncertainties have been determined from a fit to the data under the signal+background hypothesis.

## IX. SUMMARY

A search has been performed for the standard-model Higgs boson in  $9.5 \text{ fb}^{-1}$  of  $p\bar{p}$  collisions at  $\sqrt{s} = 1.96 \text{ TeV}$ , collected with the D0 detector at the Fermilab Tevatron Collider. The final state considered contains a pair of  $b$  jets and is characterized by an imbalance in transverse energy, as expected from  $p\bar{p} \rightarrow ZH \rightarrow \nu\bar{\nu}b\bar{b}$  production. The search is also sensitive to the  $WH \rightarrow \ell\nu b\bar{b}$  channel when the charged lepton is not identified. For a Higgs-boson mass of 115 GeV (125 GeV), a limit has been set at the 95% C.L. on the cross section  $\sigma(p\bar{p} \rightarrow [Z/W]H)$ , assuming standard-model branching fractions, that is a factor of 3.0 (4.3) larger than the theoretical standard-model value, for an expected factor of 2.7 (3.9).

To validate the analysis techniques, a search for WZ and ZZ production has been performed, resulting in a measurement of the combined cross section that is a factor of  $0.94 \pm 0.31(\text{stat}) \pm 0.34(\text{syst})$  relative to the standard-model prediction, and with an observed significance of  $2.0 \sigma$ , consistent with the expectation of  $2.1 \sigma$ .

## Acknowledgments

We thank the staffs at Fermilab and collaborating institutions, and acknowledge support from the DOE and NSF (USA); CEA and CNRS/IN2P3 (France); MON, Rosatom and RFBR (Russia); CNPq, FAPERJ, FAPESP and FUNDUNESP (Brazil); DAE and DST (India); Colciencias (Colombia); CONACyT (Mexico); NRF (Korea); FOM (The Netherlands); STFC and the Royal Society (United Kingdom); MSM T and GACR (Czech Republic); BMBF and DFG (Germany); SFI (Ireland); The Swedish Research Council (Sweden); and CAS and CNSF (China).

- 
- [1] M. Carena *et al.*, [arXiv:hep-ph/0010338](#); CDF and D0 Collaborations, Report No. FERMILAB-PUB-03/320-E, 2003.
  - [2] V.M. Abazov *et al.* (D0 Collaboration), Phys. Rev. Lett. **104**, 071801 (2010).
  - [3] R. Barate *et al.* (LEP Working Group for Higgs boson searches), Phys. Lett. B **565**, 61 (2003).
  - [4] G. Aad *et al.* (ATLAS Collaboration), Phys. Lett. B **710**, 49 (2012).
  - [5] S. Chatrchyan *et al.* (CMS Collaboration), Phys. Lett. B **710**, 26 (2012).
  - [6] The D0 Collaboration, D0 Note 6299-CONF (2012).
  - [7] V.M. Abazov *et al.* (D0 Collaboration), Nucl. Instrum. Methods Phys. Res. Sect. A **565**, 463 (2006); M. Abolins *et al.*, Nucl. Instrum. Methods Phys. Res. Sect. A **584**, 75 (2008); R. Angstadt *et al.*, Nucl. Instrum. Methods Phys. Res. Sect. A **622**, 298 (2010).
  - [8] C. Ochando, Report No. FERMILAB-THESIS-2008-78.
  - [9] G.C. Blazey *et al.*, [arXiv:hep-ex/0005012](#).
  - [10] V.M. Abazov *et al.* (D0 Collaboration), Phys. Rev. D **85**, 052006 (2012).
  - [11] M.L. Mangano *et al.*, J. High Energy Phys. **07**, 001 (2003); version 2.11 was used.
  - [12] T. Sjöstrand, S. Mrenna, and P. Skands, J. High Energy Phys. **05**, 026 (2006); version 6.409, D0 Tune A, was used.
  - [13] V.M. Abazov *et al.*, (D0 Collaboration), Phys. Rev. Lett. **100**, 102002 (2008).
  - [14] K. Melnikov and F. Petriello, Phys. Rev. D **74**, 114017 (2006).
  - [15] E. Boos *et al.*, Nucl. Instrum. Methods Phys. Res. Sect. A **534**, 250 (2004);  
E. Boos *et al.*, Phys. Atom. Nucl. **69**, 1317 (2006).
  - [16] J. Pumplin *et al.*, J. High Energy Phys. **07**, 012 (2002); D. Stump *et al.*, J. High Energy Phys. **10**, 046, (2003).
  - [17] R. Hamberg, W.L. van Neerven, and W.B. Kilgore, Nucl. Phys. **B359**, 343 (1991); **B644**, 403 (2002).
  - [18] A.D. Martin, R.G. Roberts, W.J. Stirling, and R.S. Thorne, Phys. Lett. B **604**, 61 (2004).
  - [19] J.M. Campbell and R.K. Ellis, Phys. Rev. D **60**, 113006 (1999).
  - [20] U. Langenfeld, S. Moch and P. Uwer, Phys. Rev. D **80**, 054009 (2009); N. Kidonakis, Phys. Rev. D **74**, 114012 (2006).
  - [21] J. Baglio and A. Djouadi, JHEP **1010**, 064 (2010).
  - [22] R. Brun and F. Carminati, CERN Program Library Long Writeup W5013, 1993 (unpublished).
  - [23] A. Schwartzman, Report No. FERMILAB-THESIS-2004-21.
  - [24] V.M. Abazov *et al.* (D0 Collaboration), Phys. Rev. Lett. **102**, 051803 (2009).
  - [25] T. Gleisberg *et al.*, J. High Energy Phys. **02** (2004) 056; J. Alwall *et al.*, Eur. Phys. J. C **53**, 473 (2008).
  - [26] V.M. Abazov *et al.* (D0 Collaboration), Nucl. Instrum. Methods in Phys. Res. Sect. A **620**, 490 (2010).
  - [27] A. Hoecker *et al.*, [arXiv:physics/0703039](#); version 4.1.0 was used.
  - [28] T. Andeen *et al.*, Report No. FERMILAB-TM-2365, 2007.
  - [29] G. Corcella *et al.*, J. High Energy Phys. **01**, 010 (2001).
  - [30] T. Junk, Nucl. Instrum. Methods Phys. Res. A **434**, 435 (1999); A. Read, J. Phys. G **28**, 2693 (2002).
  - [31] W. Fisher, Report No. FERMILAB-TM-2386-E, 2006.

TABLE I: Variables used as input to the decision trees, where the angles  $\theta$  and  $\phi$  are the polar and azimuthal angles defined with respect to the proton beam direction.  $\text{jet}_1$  refers to the leading taggable jet,  $\text{jet}_2$  refers to the next-to-leading taggable jet,  $j_{\text{all}}$  refers to any jet in the event with  $p_T > 15$  GeV and pseudorapidity  $|\eta| < 3.2$ . The thrust axis is the direction obtained from the difference of the transverse momenta of the leading and next-to-leading jets. The recoil is defined in the plane transverse to the beam using i) either the amount of missing transverse energy that remains after removal of the two leading jets, ii) or the sum of all good jet transverse momenta in the half plane opposite to the one containing the dijet system (with respect to the thrust axis). Among these two possible recoil definitions, the one that has the larger component along the direction orthogonal to the thrust is chosen.

Variables used in the MJ DT
$\Delta\phi(\text{jet}_1, \text{jet}_2)$ $\eta$ of $\text{jet}_1$ $\cancel{E}_T$ $\cancel{E}_T$ significance $\min \Delta\phi(\cancel{E}_T, j_{\text{all}})$ $\max \Delta\phi(\cancel{E}_T, j_{\text{all}}) + \min \Delta\phi(\cancel{E}_T, j_{\text{all}})$ $\max \Delta\phi(\cancel{E}_T, j_{\text{all}}) - \min \Delta\phi(\cancel{E}_T, j_{\text{all}})$ $\cancel{H}_T$ (vectorial sum of $j_{\text{all}} p_T$ ) $\cancel{H}_T / H_T$ (with $H_T$ the scalar sum of $j_{\text{all}} p_T$ ) Asymmetry between $\cancel{E}_T$ and $\cancel{H}_T$ : $(\cancel{E}_T - \cancel{H}_T) / (\cancel{E}_T + \cancel{H}_T)$ $\cancel{E}_T$ component along the thrust axis $\cancel{E}_T$ component perpendicular to the thrust axis Sum of the signed components of the dijet and recoil momenta along the thrust axis Sum of the signed components of the dijet and recoil momenta perpendicular to the thrust axis Centrality (ratio of the scalar sum of $\text{jet}_1$ and $\text{jet}_2 p_T$ to the sum of their energies) $\theta$ angle of the dijet system Polar angle of $\text{jet}_1$ boosted to the dijet rest frame with respect to the dijet direction in the laboratory
Variables used in the SM DT
Dijet mass Dijet transverse mass $\text{jet}_1 p_T$ $\text{jet}_2 p_T$ Scalar sum of $\text{jet}_1$ and $\text{jet}_2 p_T$ $\eta$ of $\text{jet}_1$ $\eta$ of $\text{jet}_2$ $\Delta\eta(\text{jet}_1, \text{jet}_2)$ $\Delta\phi(\text{jet}_1, \text{jet}_2)$ $\Delta R(\text{jet}_1, \text{jet}_2)$ $p_T$ weighted $\Delta R(\text{jet}_1, j_{\text{all}})$ $p_T$ weighted $\Delta R(\text{jet}_2, j_{\text{all}})$ $H_T$ (scalar sum of $j_{\text{all}} p_T$ ) $\cancel{H}_T$ (vectorial sum of $j_{\text{all}} p_T$ ) $\cancel{H}_T / H_T$ $\Delta\phi(\cancel{E}_T, \text{dijet})$ $\theta$ angle of $\text{jet}_1$ boosted to the dijet rest frame Polar angle of $\text{jet}_1$ boosted to the dijet rest frame with respect to the dijet direction in the laboratory $\min \Delta\phi(\cancel{E}_T, j_{\text{all}})$ $\max \Delta\phi(\cancel{E}_T, j_{\text{all}}) + \min \Delta\phi(\cancel{E}_T, j_{\text{all}})$ Dijet $p_T$ $\Delta\phi(\cancel{E}_T, \text{jet}_1)$



TABLE II: The number of expected signal, expected background and observed data events after the multijet veto, for the pre, medium and tight  $b$ -tag samples. The signal corresponds to  $m_H = 115$  GeV, “Top” includes pair and single top quark production, and  $VV$  is the sum of all diboson processes. The uncertainties quoted arise from the statistics of the simulation and from the sources of systematic uncertainties mentioned in the text.

Sample	$ZH$	$WH$	$W$ +jets	$Z$ +jets	Top	$VV$	Multijet	Total Background	Observed
Pre $b$ -tag	$26.8 \pm 2.7$	$25.4 \pm 2.5$	66895	25585	1934	3144	1977	$99535 \pm 12542$	98980
Medium $b$ -tag	$9.9 \pm 1.0$	$9.3 \pm 0.9$	3112	1074	761	237	278	$5462 \pm 776$	5453
Tight $b$ -tag	$8.7 \pm 1.1$	$8.1 \pm 1.0$	443	252	377	56	6	$1134 \pm 192$	1039

TABLE III: Systematic uncertainties, in percent, of the overall signal and background yields. “Jet EC” and “Jet ER” stand for jet energy calibration and resolution respectively. “Jet R&T” stands for jet reconstruction and taggability. “Signal” includes  $ZH$  and  $WH$  production and is shown for  $m_H = 115$  GeV.

Systematic Uncertainty	Signal (%)	Background (%)
Medium $b$ -tag		
Jet EC - Jet ER	$\pm 0.9$	$\pm 1.9$
Jet R&T	$\pm 2.9$	$\pm 2.9$
$b$ Tagging	$\pm 0.6$	$\pm 3.7$
Trigger	$\pm 2.0$	$\pm 1.9$
Lepton Identification	$\pm 0.9$	$\pm 0.9$
Heavy Flavor Fractions	—	$\pm 8.5$
Cross Sections	$\pm 7.0$	$\pm 9.8$
Luminosity	$\pm 6.1$	$\pm 5.8$
Multijet Normalization	—	$\pm 1.2$
Total	$\pm 10.0$	$\pm 14.2$
Tight $b$ -tag		
Jet EC - Jet ER	$\pm 1.3$	$\pm 1.8$
Jet R&T	$\pm 2.7$	$\pm 3.1$
$b$ Tagging	$\pm 7.8$	$\pm 7.4$
Trigger	$\pm 2.0$	$\pm 2.0$
Lepton Identification	$\pm 0.8$	$\pm 1.1$
Heavy Flavor Fractions	—	$\pm 11.1$
Cross Sections	$\pm 7.0$	$\pm 10.0$
Luminosity	$\pm 6.1$	$\pm 6.1$
Multijet Normalization	—	$\pm 0.1$
Total	$\pm 12.7$	$\pm 16.9$

TABLE IV: The observed and expected upper limits measured using  $9.5 \text{ fb}^{-1}$  of data on the  $(W/Z)H$  production cross section relative to the SM expectation as a function of  $m_H$ .

$m_H$	100	105	110	115	120	125	130	135	140	145	150
Expected	2.06	2.20	2.44	2.70	3.22	3.90	5.04	6.65	9.16	13.8	21.6
Observed	1.93	2.25	2.19	2.96	3.47	4.29	4.28	7.16	8.81	15.3	16.8

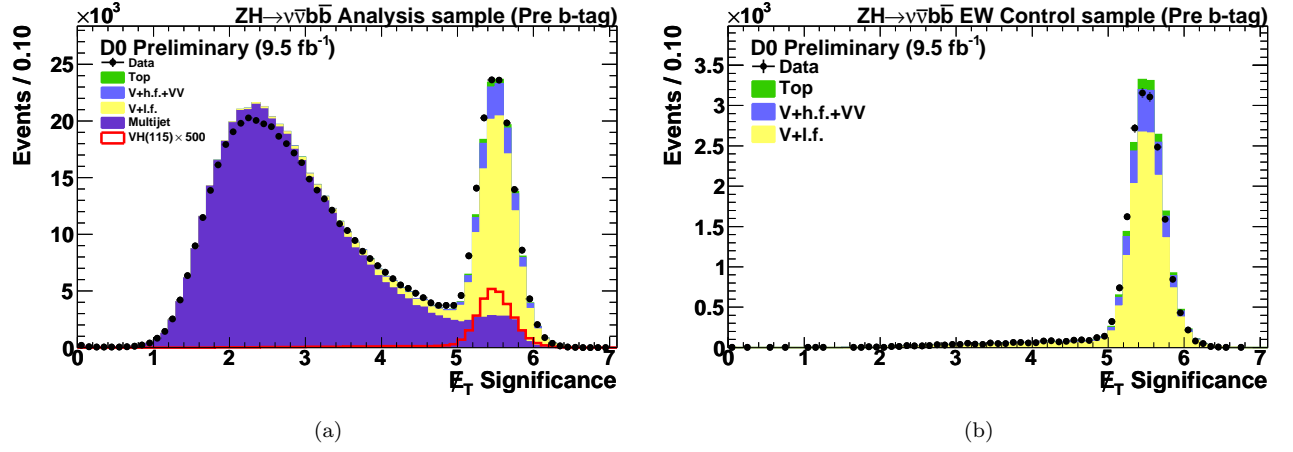


FIG. 1: Missing  $E_T$  significance in (a) the analysis and (b) the EW-control samples without the requirement that the significance be larger than 5. The data are shown as points and the background contributions as histograms: dibosons are labeled as “VV,” “V+l.f.” includes  $(W/Z)+(u, d, s, g)$  jets, “V+h.f.” includes  $(W/Z)+(b, c)$  jets and “Top” includes pair and single top quark production. In (a), the distribution for signal (VH) is multiplied by a factor of 500 and includes  $ZH$  and  $WH$  production for  $m_H = 115$  GeV.

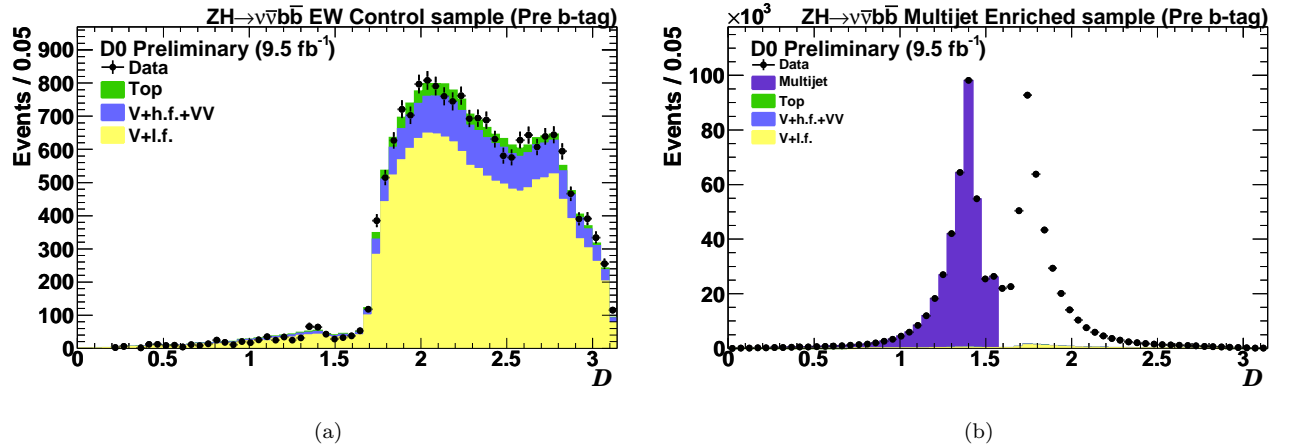


FIG. 2: Distribution of  $\mathcal{D}$  in (a) the EW-control sample and (b) the MJ-enriched sample, without the requirement that it be larger than  $\pi/2$ . The data are shown as points and the background contributions as histograms: dibosons are labeled as “VV,” “V+l.f.” includes  $(W/Z)+(u, d, s, g)$  jets, “V+h.f.” includes  $(W/Z)+(b, c)$  jets and “Top” includes pair and single top quark production. In (b), the shaded region ( $\mathcal{D} < \pi/2$ ) is used to model the events in the unshaded region ( $\mathcal{D} > \pi/2$ ); the dip observed in the region around  $\pi/2$  is due to the acoplanarity cut between the Higgs candidate jets. These distributions are shown before  $b$  tagging.

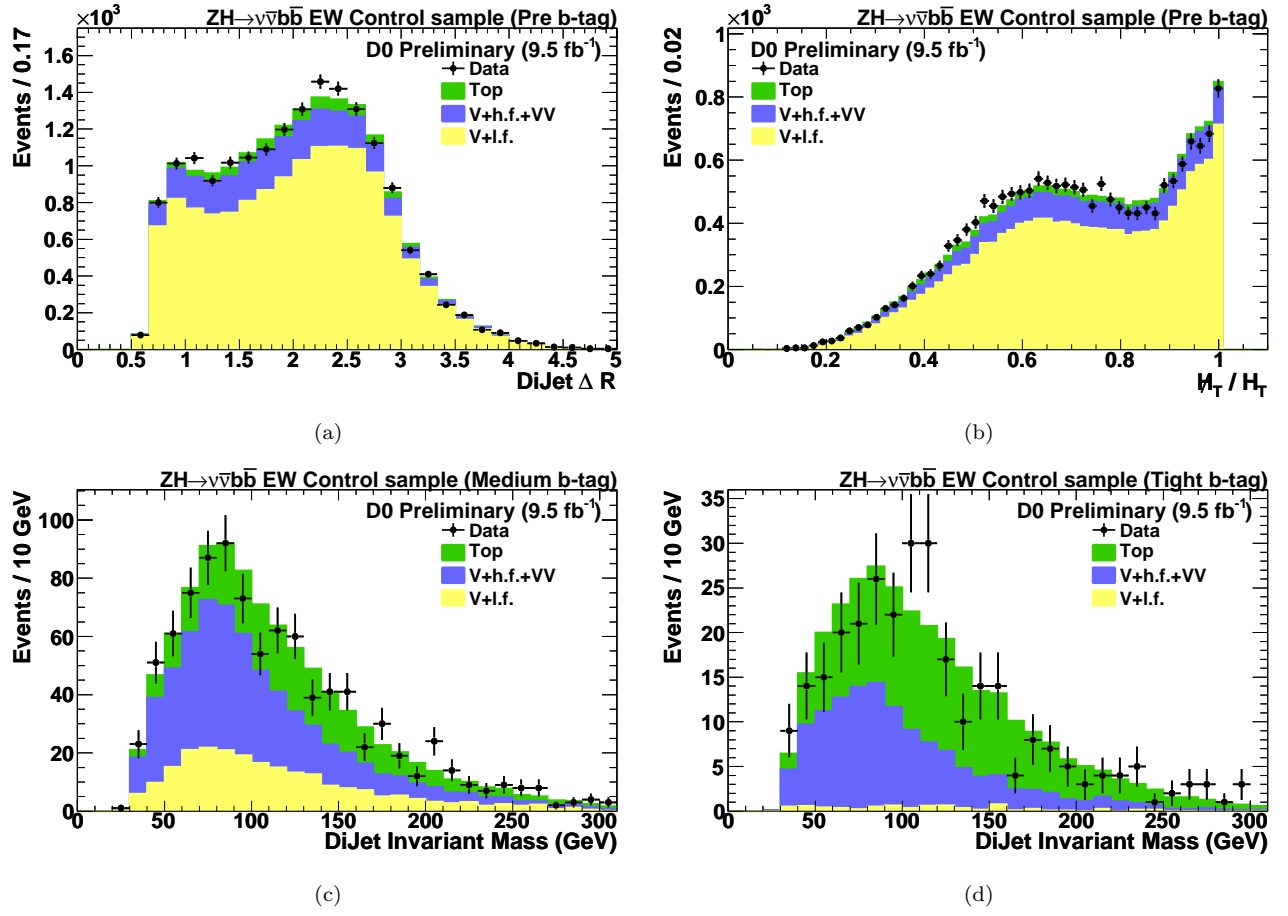


FIG. 3: Representative variable distributions in the EW-control sample: (a) dijet  $\Delta R$  in the pre  $b$ -tag sample, (b)  $H_T/H_T$  (defined in Table I) in the pre  $b$ -tag sample, (c) dijet invariant mass in the medium  $b$ -tag sample, (d) dijet invariant mass in the tight  $b$ -tag sample. The data are shown as points and the background contributions as histograms: dibosons are labeled as “VV,” “V+l.f.” includes  $(W/Z)+(u, d, s, g)$  jets, “V+h.f.” includes  $(W/Z)+(b, c)$  jets and “Top” includes pair and single top quark production.

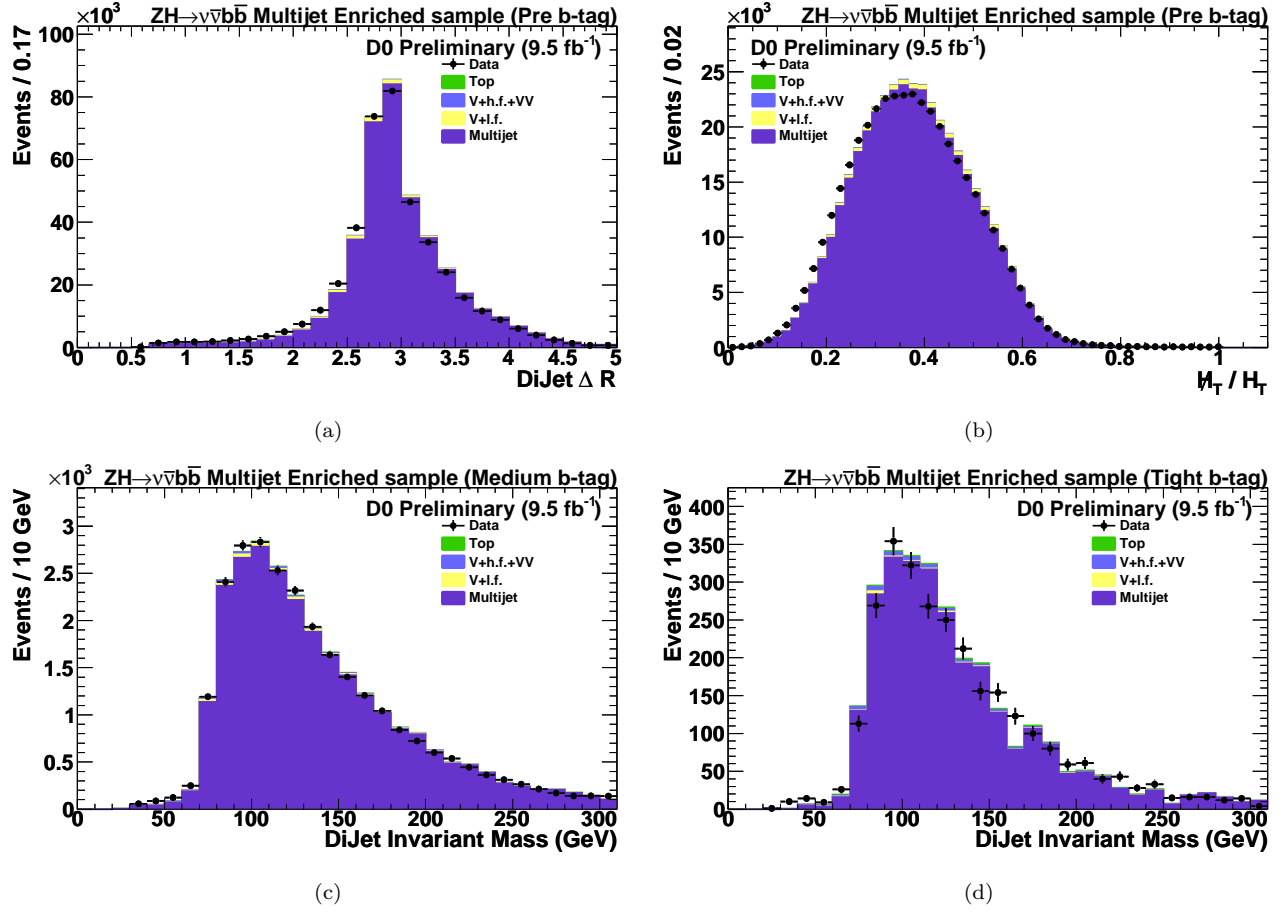


FIG. 4: Representative variable distributions in the MJ-enriched sample: (a) dijet  $\Delta R$  in the pre  $b$ -tag sample, (b)  $H_T/H_T$  (defined in Table I) in the pre  $b$ -tag sample, (c) dijet invariant mass in the medium  $b$ -tag sample, (d) dijet invariant mass in the tight  $b$ -tag sample. The data with  $\mathcal{D} > \pi/2$  are shown as points and the background contributions as histograms: dibosons are labeled as “VV,” “V+l.f.” includes  $(W/Z)+(u, d, s, g)$  jets, “V+h.f.” includes  $(W/Z)+(b, c)$  jets and “Top” includes pair and single top quark production. The “multijet” histogram is obtained from the data with  $\mathcal{D} < \pi/2$

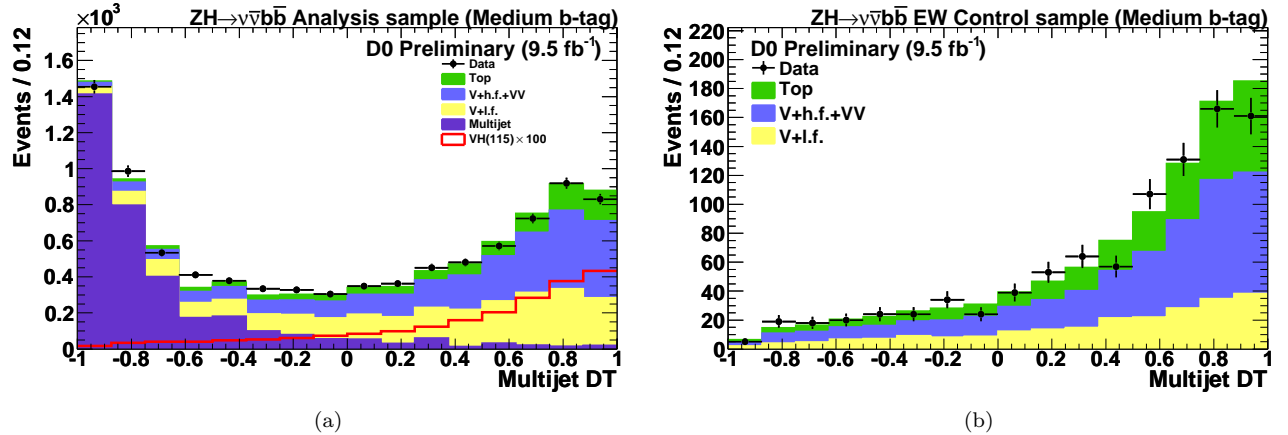


FIG. 5: MJ DT output after the medium  $b$ -tagging requirement in the (a) analysis sample and (b) EW-control sample. The distribution for signal (VH), shown for  $m_H = 115$  GeV, is multiplied by a factor of 100 and includes  $ZH$  and  $WH$  production. The data are shown as points and the background contributions as histograms: dibosons are labeled as “VV,” “V+l.f.” includes  $(W/Z)+(u, d, s, g)$  jets, “V+h.f.” includes  $(W/Z)+(b, c)$  jets and “Top” includes pair and single top quark production.

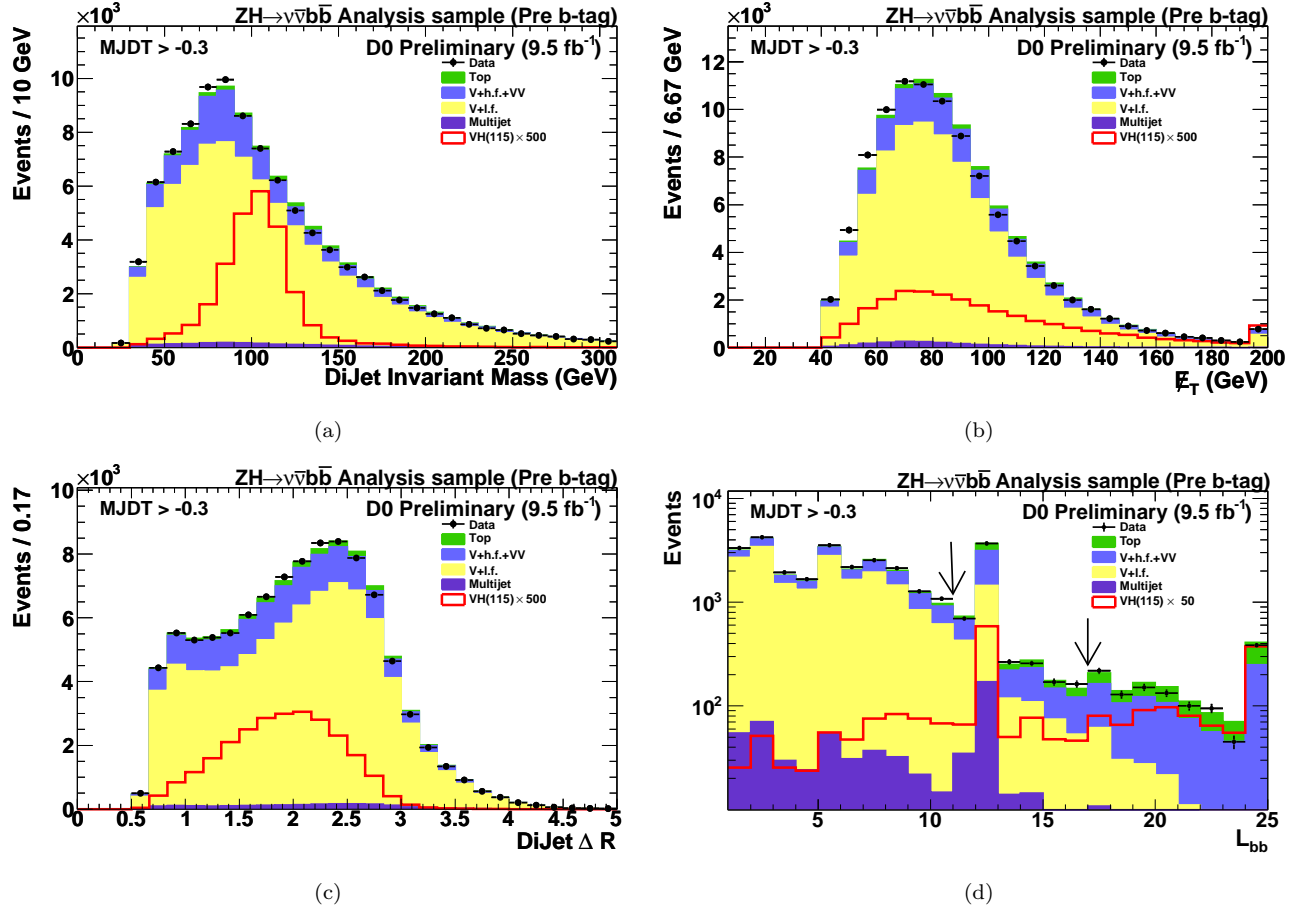


FIG. 6: Representative variable distributions in the analysis sample after the multijet veto and before any  $b$  tagging requirement: (a) dijet invariant mass, (b) missing  $E_T$ , (c) dijet  $\Delta R$ , (d)  $b$ -tagging discriminating variable ( $L_{bb}$ ). The bin at zero is suppressed in this plot due to the large number of entries, mostly from pairs of light jets. The relatively high number of events observed at  $L_{bb} = 12$  comes mainly from events with one untagged jet and one very tightly  $b$ -tagged jet; the one at  $L_{bb} = 24$  comes from events with two very tightly  $b$ -tagged jets. The vertical arrows indicate the thresholds used to define the  $b$ -tag samples. The distributions for signal (VH), which are multiplied by a factor of 500 for (a)–(c) and 50 for (d), include  $ZH$  and  $WH$  production for  $m_H = 115$  GeV. The data are shown as points and the background contributions as histograms: dibosons are labeled as “VV,” “V+l.f.” includes  $(W/Z)+(u, d, s, g)$  jets, “V+h.f.” includes  $(W/Z)+(b, c)$  jets and “Top” includes pair and single top quark production.

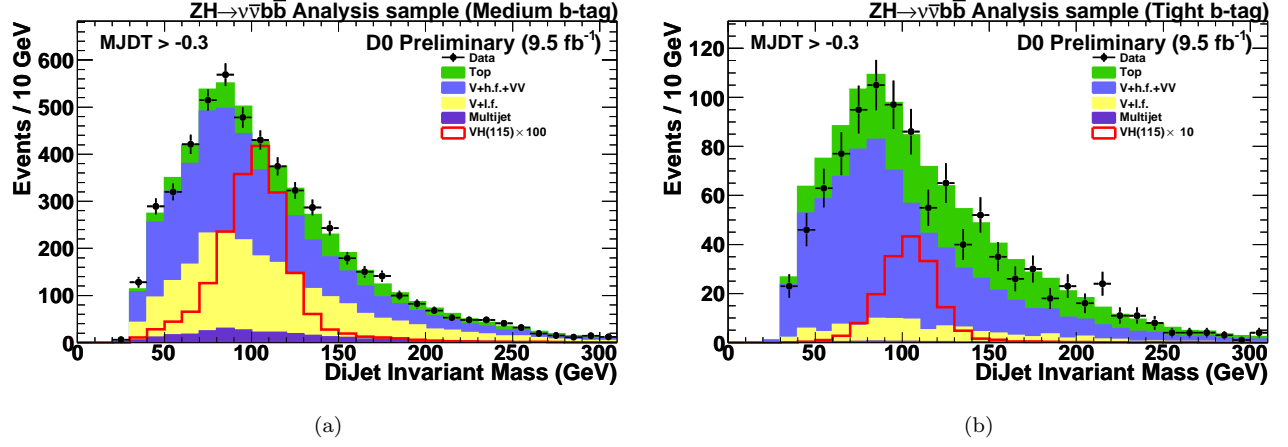


FIG. 7: Dijet invariant mass in the analysis sample after the multijet veto for (a) medium  $b$ -tag and (b) tight  $b$ -tag. The distributions for signal (VH), which are multiplied by a factor of 100 for medium  $b$ -tag and 10 for tight  $b$ -tag respectively, include  $ZH$  and  $WH$  production for  $m_H = 115$  GeV. The data are shown as points and the background contributions as histograms: dibosons are labeled as “VV,” “V+l.f.” includes  $(W/Z)+(u, d, s, g)$  jets, “V+h.f.” includes  $(W/Z)+(b, c)$  jets and “Top” includes pair and single top quark production.

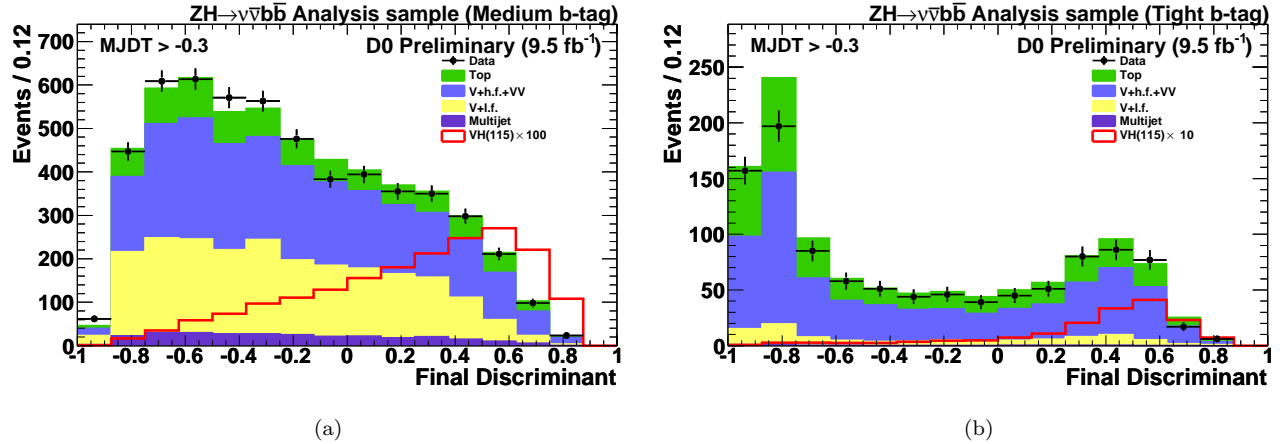


FIG. 8: The SM DT output for the VH search where  $m_H = 115$  GeV following the multijet veto for (a) medium  $b$ -tag and (b) tight  $b$ -tag prior to the fit to data. The distributions for signal are multiplied by a factor of 100 for medium  $b$ -tag and 10 for tight  $b$ -tag, respectively, and include  $ZH$  and  $WH$  production for  $m_H = 115$  GeV. The data are shown as points and the background contributions as histograms: dibosons are labeled as “VV,” “V+l.f.” includes  $(W/Z)+(u, d, s, g)$  jets, “V+h.f.” includes  $(W/Z)+(b, c)$  jets and “Top” includes pair and single top quark production.

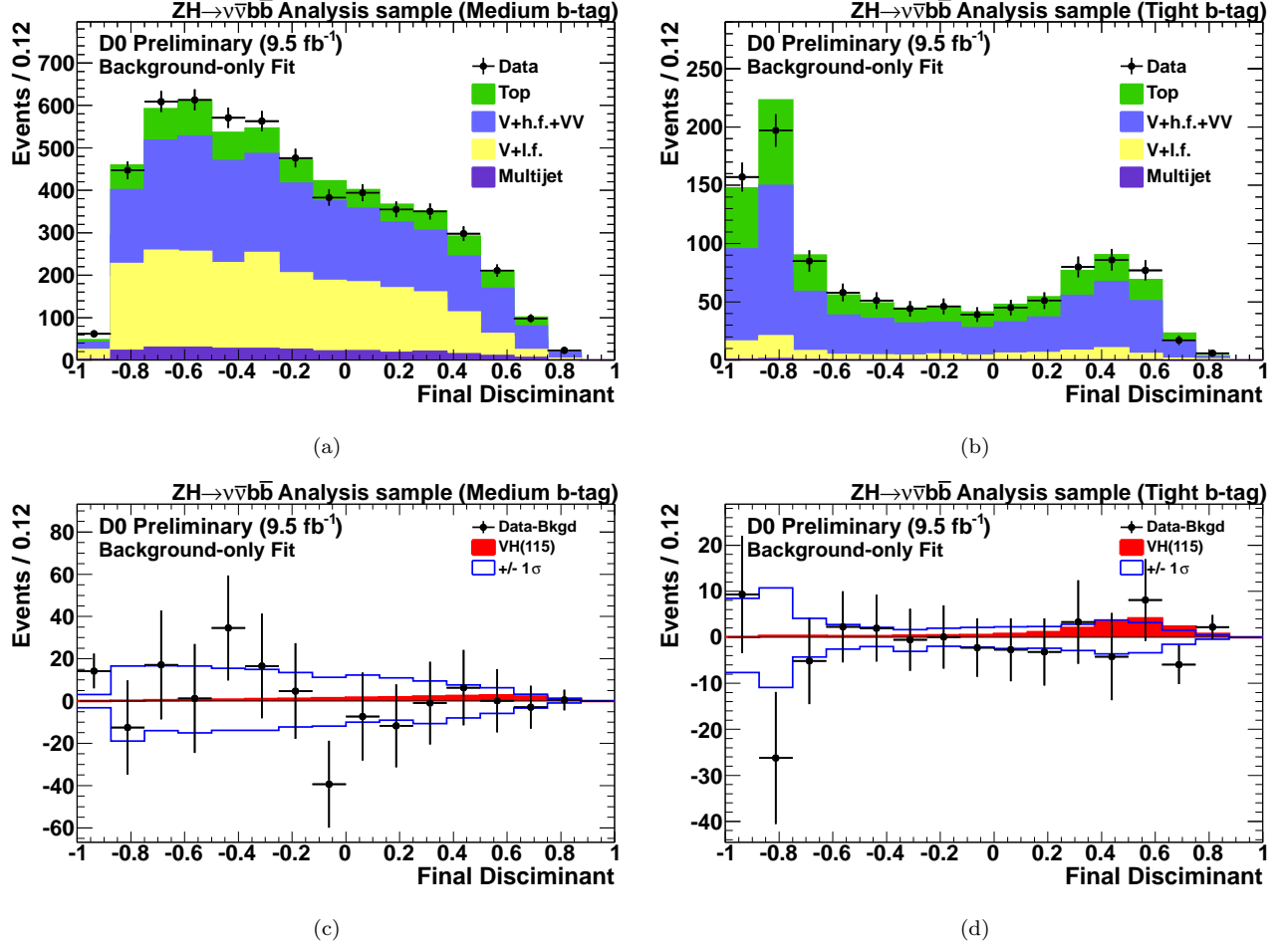
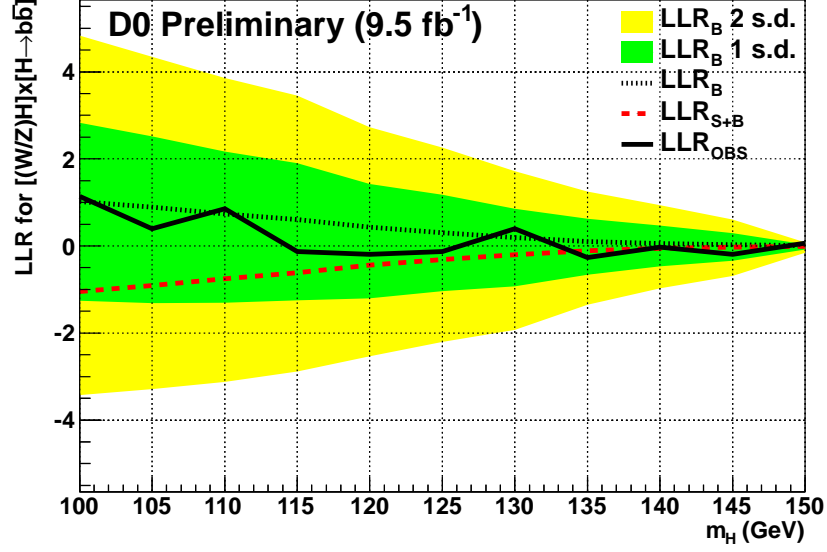
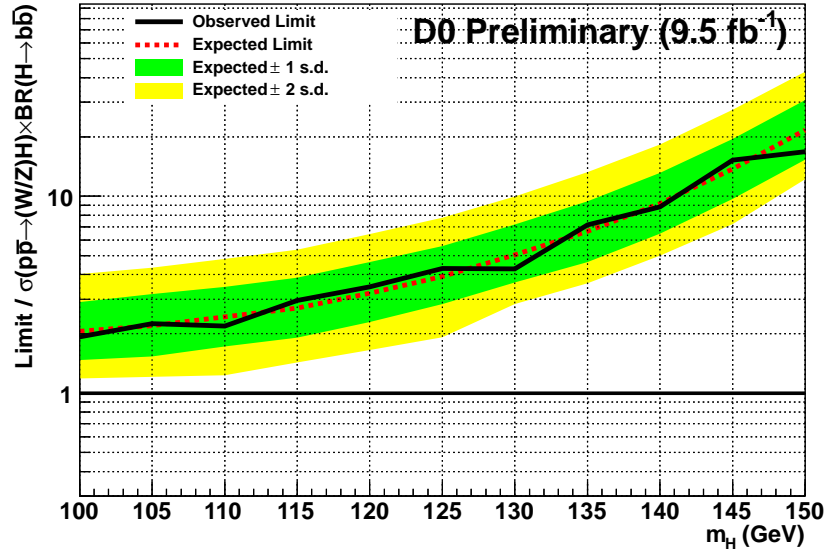


FIG. 9: The SM DT output, for  $m_H = 115$  GeV, following the multijet veto and after the fit to the data under the background-only hypothesis in the (a) medium and (b) tight  $b$ -tag channels. The data are shown as points and the background contributions as histograms: dibosons are labeled as “VV”, “V+l.f.” includes  $(W/Z)+(u, d, s, g)$  jets, “V+h.f.” includes  $(W/Z)+(b, c)$  jets and “Top” includes pair and single top quark production. The SM VH signal expectation (red histogram) and the data after subtracting the fitted background (points) are shown in the (c) medium and (d) tight tag channels. Also shown is the  $\pm 1$  standard deviation band on the total background after fitting. No scaling factor is applied to the signal.



(a)



(b)

FIG. 10: (a) The observed (solid black) and expected LLRs for the background-only (black dots) and signal+background hypotheses (red dashes). (b) Ratio of the observed (solid black) and expected (dotted red) exclusion limits to the SM production cross section for the VH search. Both are shown as a function of  $m_H$  with the heavy green and light yellow shaded areas corresponding to the 1 and 2 standard deviations (s.d.) around the background-only hypothesis.



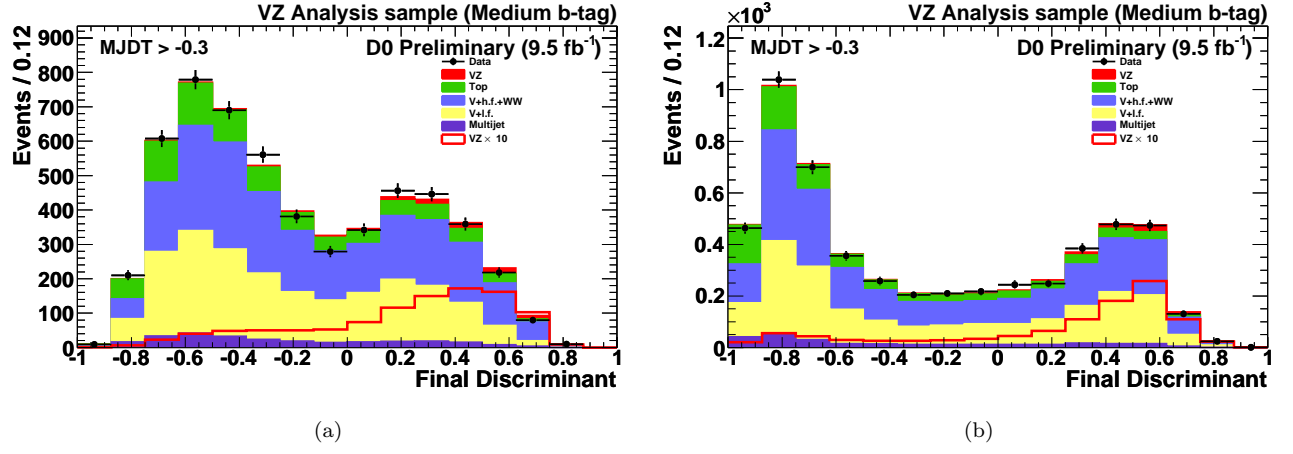


FIG. 11: The SM DT output for the  $WZ$  and  $ZZ$  diboson search following the multijet veto for (a) medium and (b) tight tag prior to the fit to data. The data are shown as points and the background contributions as histograms; “V+l.f.” includes  $(W/Z)+(u, d, s, g)$  jets, “V+h.f.” includes  $(W/Z)+(b, c)$  jets and “Top” includes pair and single top quark production. The  $WZ$  and  $ZZ$  signal is denoted as  $VZ$ . The distributions for signal are scaled to the SM cross section (filled red histogram) or multiplied by a factor of 10 for medium tag and 5 for tight tag (solid red line) respectively,

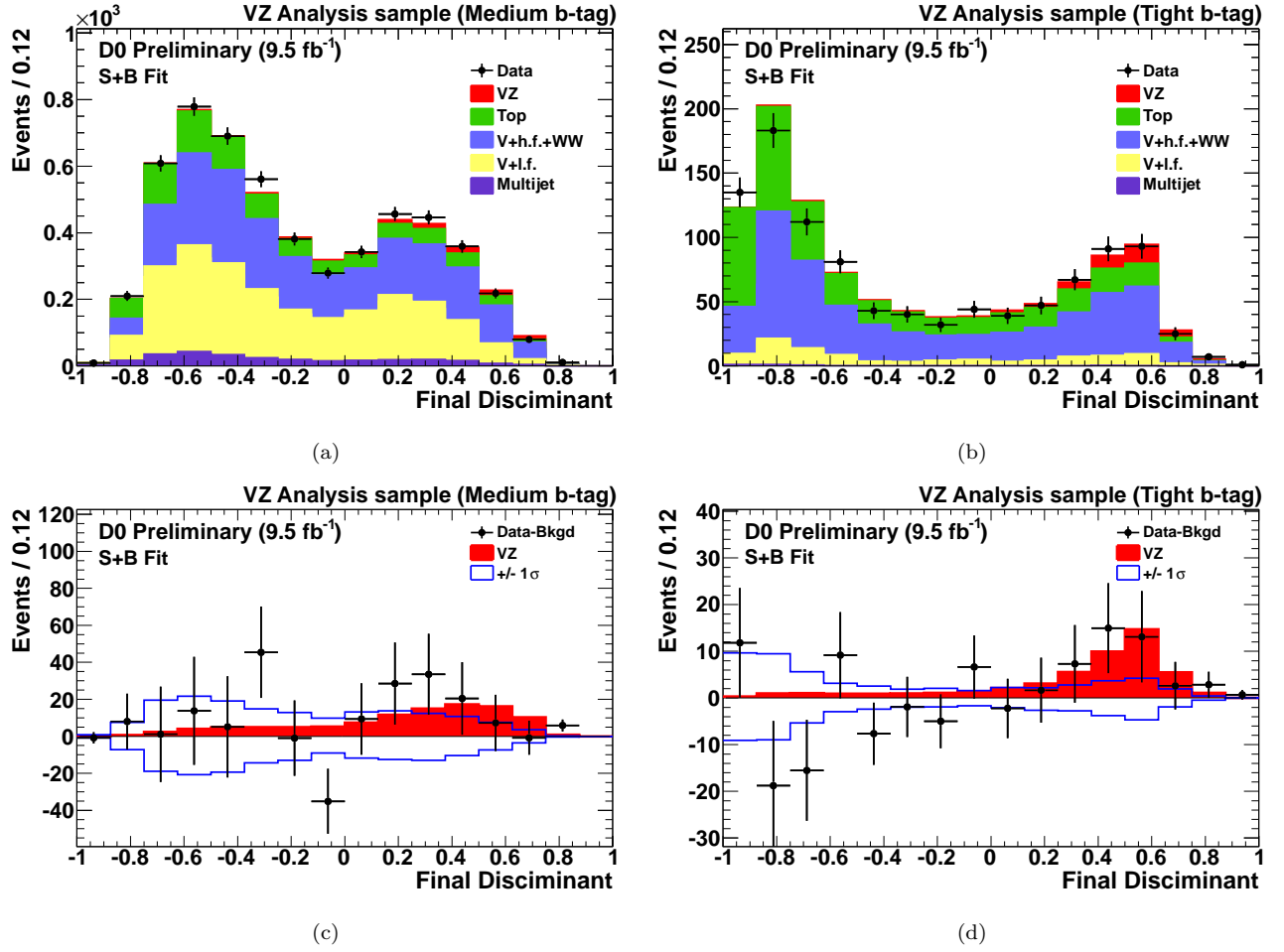


FIG. 12: The SM DT output for the  $WZ$  and  $ZZ$  diboson search, following the multijet veto, and after the fit to the data under the signal+background hypothesis in the (a) medium and (b) tight tag channels. The data are shown as points and the background contributions as histograms; “V+l.f.” includes  $(W/Z)+(u, d, s, g)$  jets, “V+h.f.” includes  $(W/Z)+(b, c)$  jets and “Top” includes pair and single top quark production. The  $WZ$  and  $ZZ$  signal expectation (red histogram, and denoted VZ) and the data after subtracting the fitted background (points) are shown in the (c) medium and (d) tight tag channels. Also shown is the  $\pm 1$  standard deviation band on the total background after fitting. The signal is scaled to the SM cross section.

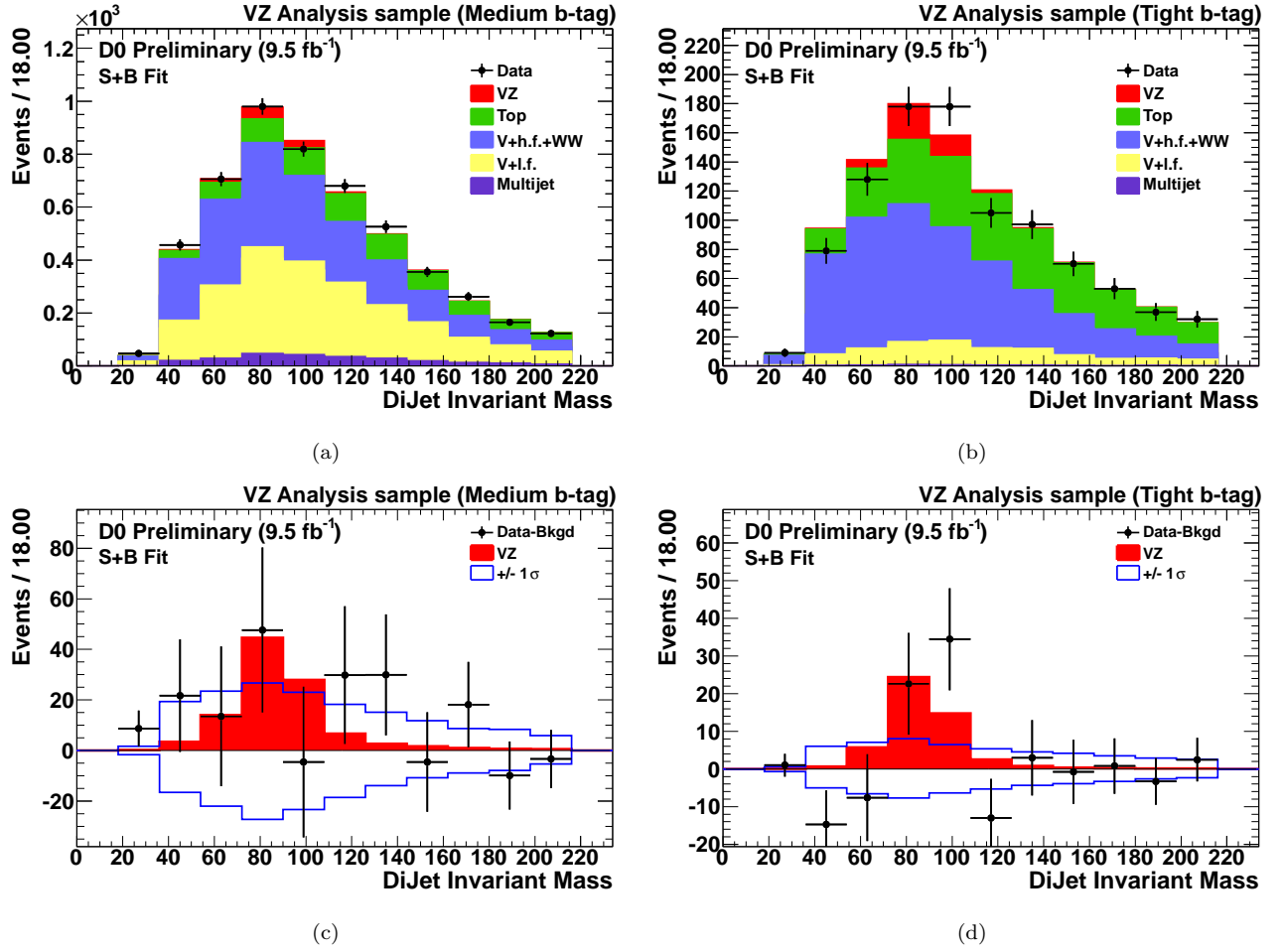


FIG. 13: The dijet invariant mass for the  $WZ$  and  $ZZ$  diboson search, following the multijet veto, and after the fit to the data under the signal+background hypothesis in the (a) medium and (b) tight tag channels. The data are shown as points and the background contributions as histograms; “V+l.f.” includes  $(W/Z)+(u, d, s, g)$  jets, “V+h.f.” includes  $(W/Z)+(b, c)$  jets and “Top” includes pair and single top quark production. The  $WZ$  and  $ZZ$  signal expectation (red histogram, and denoted VZ) and the data after subtracting the fitted background (points) are shown in the (c) medium and (d) tight tag channels. Also shown is the  $\pm 1$  standard deviation band on the total background after fitting. The signal is scaled to the SM cross section.

## APPENDIX A: COMPARISON WITH PREVIOUS RESULTS

In this appendix we make a comparison of these results to the previous version of this analysis [6]. The changes in the expected limits are shown in Fig. 14(a), and the changes in the observed limits are shown in Fig 14(b). The expected limits have improved by around 10% across the tested mass range. The most notable change in the observed limits is that the new limits fluctuate less from mass to mass. These changes are primarily due to improved separation of the signal from the background in the final discriminants after significantly increasing Monte Carlo statistics used in the training. This improvement is illustrated in Fig. 15, which shows the signal efficiency versus background rejection ( $1/\text{efficiency}$ ) for an arbitrary cut on the final discriminants from the current and previous iterations of the analysis.

Because this analysis divides the data into multiple channels (medium and tight  $b$ -tag for four data periods), it is useful when trying to understand the final limits to collect the distributions from the individual channels into a single distribution. To preserve the sensitivity from the bins with high signal-to-background ratios ( $s/b$ ), only bins with similar  $s/b$  are combined. Thus we construct an aggregate distribution by re-ordering the bins from the input distributions according to  $\ln(s/b)$ . Figure 16 shows the highest  $s/b$  region of the aggregate distribution for this analysis and for the analysis from Ref. [6]. Relative to that previous analysis, we now expect more events in the highest  $\ln(s/b)$  bins, and the maximum  $s/b$  is slightly higher. Figure 17 shows the same distributions after subtraction of the background. Integrating the distributions in Fig. 16 from *right to left* (i.e. starting from the highest  $s/b$  events) allows one to see how the data compare to the background-only and signal+background hypotheses as the most significant events are accumulated. Figure 18 shows these cumulative distributions for the  $\approx 150$  most significant events as a function of the integrated number of predicted signal events. Here we can again see that slightly more signal is integrated for the same amount of background.

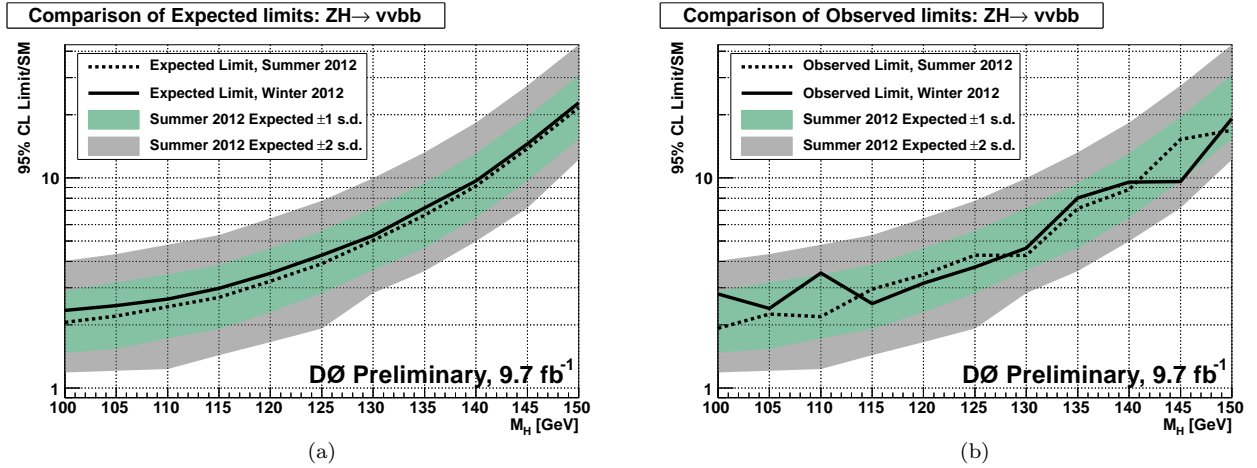


FIG. 14: Comparison of (a) expected, and (b) observed limits for this result (dashed line), and the result from Ref. [6] (solid line). In both cases, the bands represent 1 and 2 standard deviation (s.d.) around the expected limit for the current analysis.

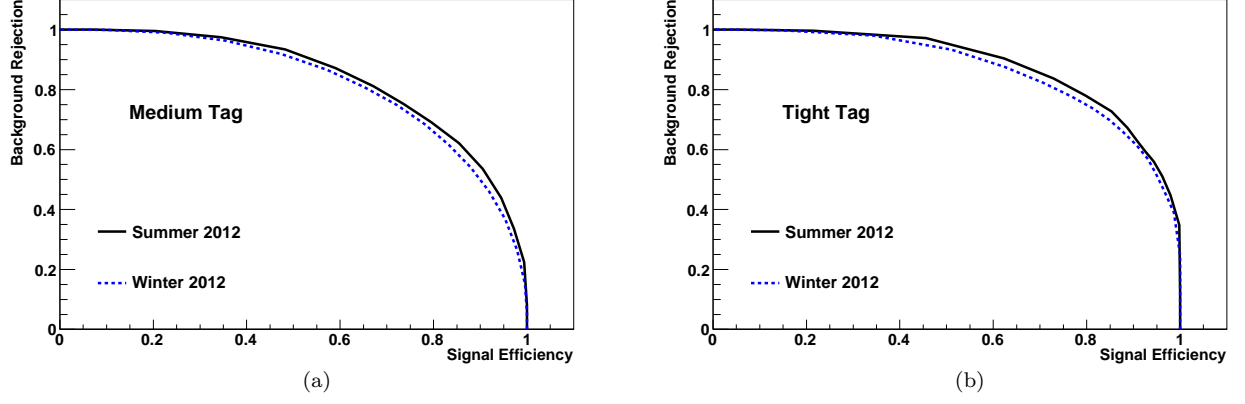


FIG. 15: Signal efficiency versus background rejection ( $1/\text{efficiency}$ ) when cutting on (a) the medium tag or (b) tight tag final discriminants for a Higgs boson mass of 125 GeV. The solid black lines are for the discriminants in this analysis and the dashed blue lines are for the analysis in Ref. [6].

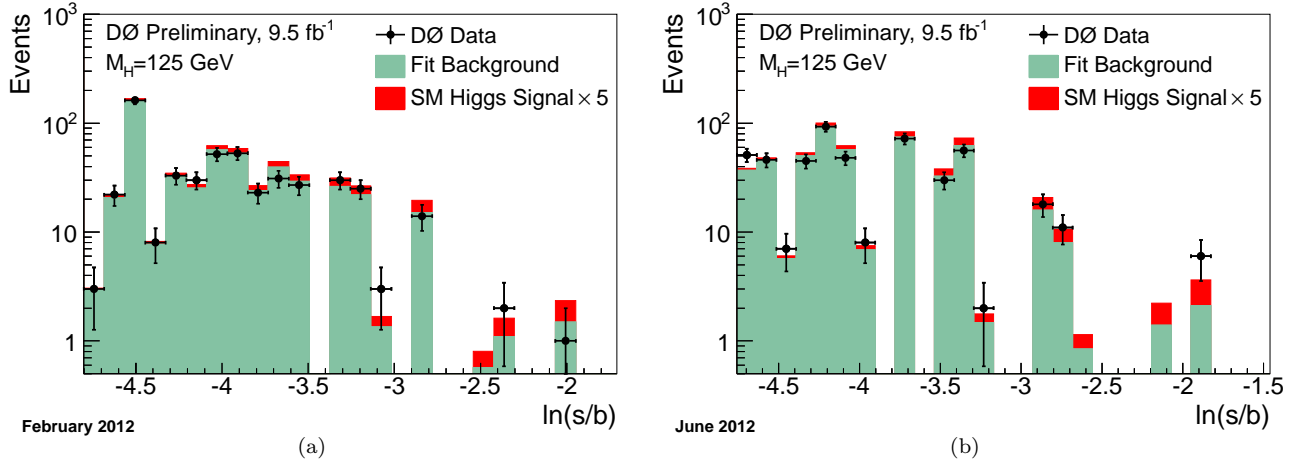


FIG. 16: Distributions of  $\ln(s/b)$  from (a) the results in Ref. [6] and from (b) this analysis for a Higgs boson mass of 125 GeV. The signal has been scaled by a factor of five. The data are shown with points and the expected signal is stacked on top of the sum of backgrounds.

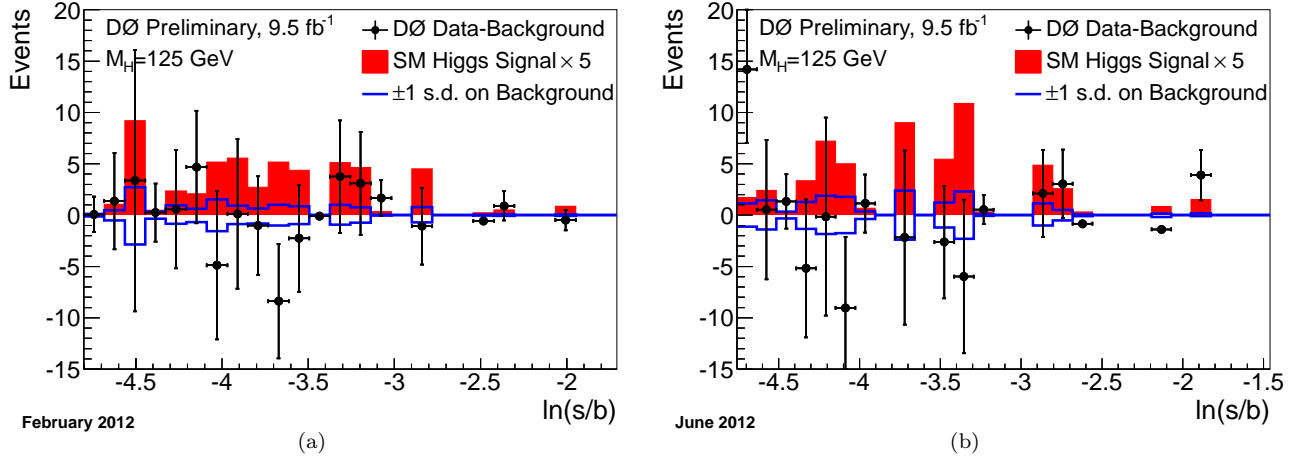


FIG. 17: Distributions of  $\ln(s/b)$  with the background subtracted from the data for (a) the results in Ref. [6] and (b) this analysis, for a Higgs boson mass of 125 GeV. The background subtracted data are shown as points and the signal, scaled by a factor of five, is shown as the red histograms. The blue lines indicate the uncertainty on the background prediction.

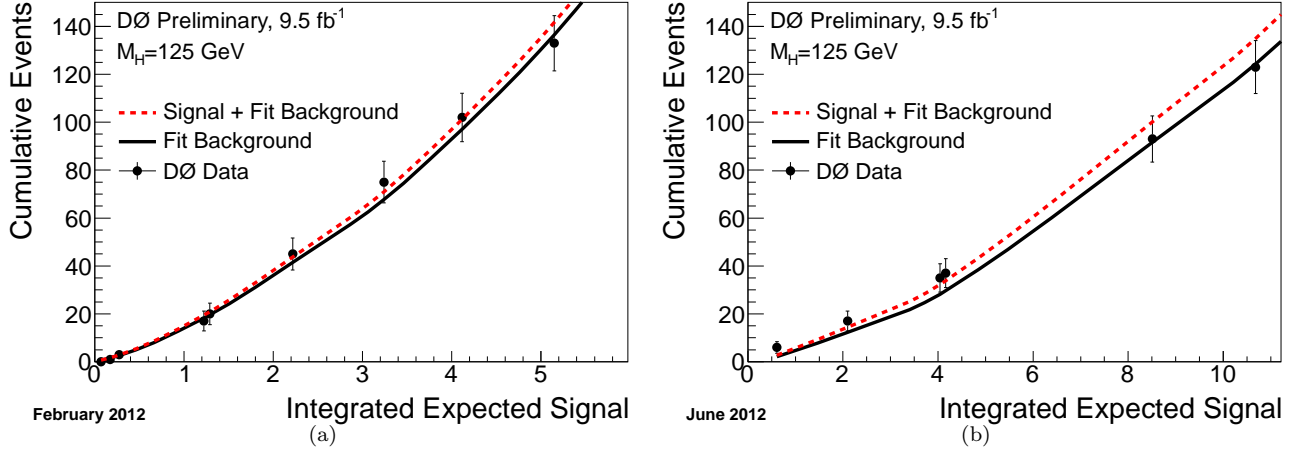


FIG. 18: Cumulative number of events for the highest  $s/b$  bins for  $M_H = 125$  GeV for (a) the results in Ref. [6] and (b) this analysis. The integrated background-only and signal+background predictions are shown as a function of the accumulated number of signal events. The points show the integrated number of events observed.

## APPENDIX B: RESULTS FROM SIGNAL INJECTION

In Fig. 19, the median expected LLRs for the background only and signal+background hypotheses are the same as in Fig. 10a, while the LLR observed in data has been replaced by the median expected LLR in the presence of a Higgs boson with a mass of 125 GeV.

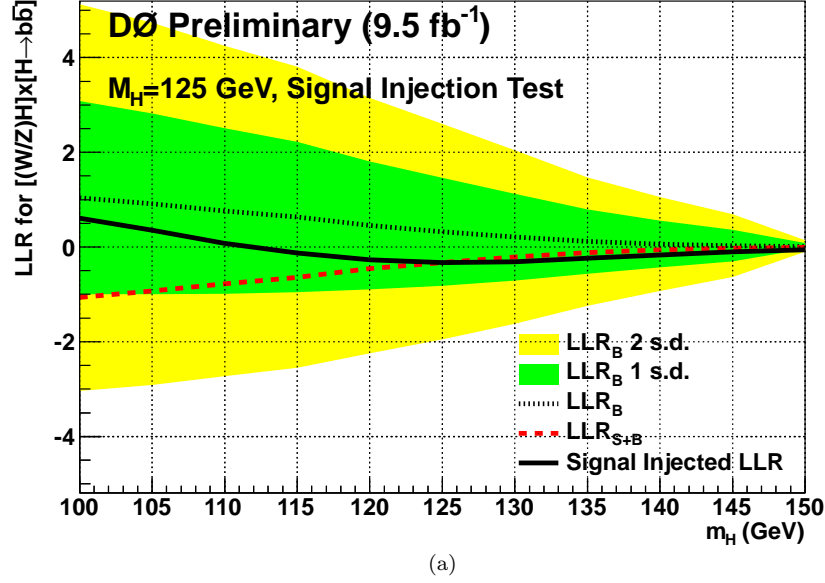


FIG. 19: The LLRs expected in the presence of a Higgs boson with  $m_H = 125$  GeV (solid black), expected for the background-only (black dots) and signal+background hypotheses (red dashes), shown as a function of the tested values of  $m_H$  with the heavy green and light yellow shaded areas corresponding to the 1 and 2 standard deviations (s.d.) around the background-only hypothesis.